The paper was published in the proceedings of the 11th International Conference on Physical Modelling in Geotechnics (ICPMG2026) and was edited by Ioannis Anastasopoulos. The conference was held from June 8th to June 12th 2026 in Zurich, Switzerland.

Numerical Investigation on the Ultimate Lateral Resistance of Steel Pipe Piles Failing Due to Axial Force Fluctuations Induced by Overturning Moments of Superstructures

M. Sato
Tohoku University, Sendai City, Japan, sato.mutsuki.t7@dc.tohoku.ac.jp

Y. Kimura
Tohoku University, Sendai City, Japan, kimura@tohoku.ac.jp

ABSTRACT: Steel is a material with high strength and ductility, making steel pipe piles suitable for use as foundations for various structures due to their superior load-bearing and deformation capacities. However, thin-walled steel pipes are susceptible to local buckling when subjected to bending under high compressive axial forces. If buckling occurs, the pile may fail before exhibiting its inherent material capacity. Local buckling is therefore known to reduce the structural performance of steel members, particularly in terms of strength and ductility. In high-rise buildings, large overturning moments during earthquakes can cause substantial variations in axial force on piles, raising concerns that local buckling may compromise the structural performance of pile foundations. This issue is especially critical in performance-based design, where piles are expected to sustain damage while still providing structural integrity. If local buckling occurs, the intended performance may not be achieved, potentially affecting building safety. This study investigates the effect of axial force variation induced by overturning moments on the ultimate lateral resistance of steel pipe piles. Centrifuge model tests are conducted to reproduce the failure process of piles under lateral loading. A FEA model simulating the experimental setup is then developed and validated. Using the model, a parametric study is performed to examine how axial force variation influences the ultimate lateral resistance. The findings contribute to better understanding and evaluation of structural performance in pile foundations subject to complex loading conditions, particularly for steel piles with high ductility.

1 INTRODUCTION

In the 2024 Noto Peninsula Earthquake, several superstructures overturned due to strong overturning moments (National Institute for Land and Infrastructure Management & Building Research Institute, 2024). In Japan, foundation design has long been based on elastic design principles (AIJ, 2001). Within the range of design loads, elastic design keeps structures almost undamaged and appears to be a robust design approach. However, once the applied load exceeds the design load, the collapse mechanism of the structure becomes uncertain. Therefore, large-scale collapse mechanisms such as those mentioned above are nearly impossible to predict at the design stage.

Since 2019, the second-level design concept has been introduced as a design method that considers potential collapse mechanisms (AIJ, 2019). This enables designers to anticipate and avoid undesirable collapse mechanisms in advance. In the second-level design, partial plastic deformation of members is permitted within the design load range. Steel materials are known to exhibit stable hysteretic behavior even after yielding (Kimura et al., 2013), in contrast to concrete, which tends to fail in a brittle manner. From this perspective, steel pipe piles are highly compatible with the second-level design concept.

However, compared with concrete piles that have dense cross-sections, thin-walled steel pipe piles are susceptible to local buckling under high axial forces (Sato et al., 2025). Under strong overturning moments, axial forces acting on piles may reach approximately twice the long-term load. In pile groups supporting building foundations, the front-row piles in the loading direction are most affected by overturning moments. In general, the leading piles in the loading direction tend to carry the largest portion of the applied load. If local buckling occurs at the pile head, the apparent stiffness of the member decreases, leading to a reduction in the load-carrying capacity under the same displacement. Many previous studies have not considered nonlinear phenomena such as geometric nonlinearity or plastic deformation of piles (Kashiwa et al., 2007). Furthermore, the load-sharing ratio among piles has typically been evaluated using empirical formulas in which only pile diameter and spacing are treated as variables (AIJ, 2019).

Based on these considerations, centrifuge loading experiments were conducted in this study. The centrifuge tests aimed to capture the process by which the pile foundation approaches its ultimate state under overturning moments transmitted from the superstructure. In addition, FEA were performed to extend the range of parameters investigated in the experiments. The analysis introduced the height of the loading point as a variable to highlight the influence of overturning moments. Under these conditions, the ultimate lateral resistance of the pile foundation and the load-sharing characteristics among piles were examined.

2 CENTRIFUGE LOADING TEST

This chapter presents an overview of the centrifuge loading experiments conducted in this study. The objective of the experiments was to reproduce the process in which local buckling occurs in the piles and leads to overall collapse. The tests were performed using the centrifuge facility at the Disaster Prevention Research Institute, Kyoto University.

2.1 Overview of the Loading Test

Figure 1 illustrates the setup of the test model. The scale ratio of the model is 1/50. The test model consists of (1) a weight simulating the superstructure, (2) two piles, and (3) a dry sandy soil bed composed of Toki silica sand No. 7. The soil was prepared by the air pluviation method in twelve layers, with a relative density Dr = 40%. The piles were made of aluminum. Axial forces were applied to the piles by the self-weight of the superstructure. In this test, the weight of the superstructure was adjusted so that the initial axial force N_0 was approximately 0.4 N_y, where N_y denotes the yield axial force of the pile. This value was determined based on the typical axial force ratio reported in previous reports (Mukai et al., 2019). The superstructure was pin-connected through a load cell and was subjected to lateral loading from the side by an actuator, as shown in the figure. The loading point was positioned 20 mm above the ground surface in model scale. Two displacement transducers were installed on the side and on the top of the superstructure.

Figure 2 illustrates the arrangement of strain gauges attached to the piles. The strain gauges on the

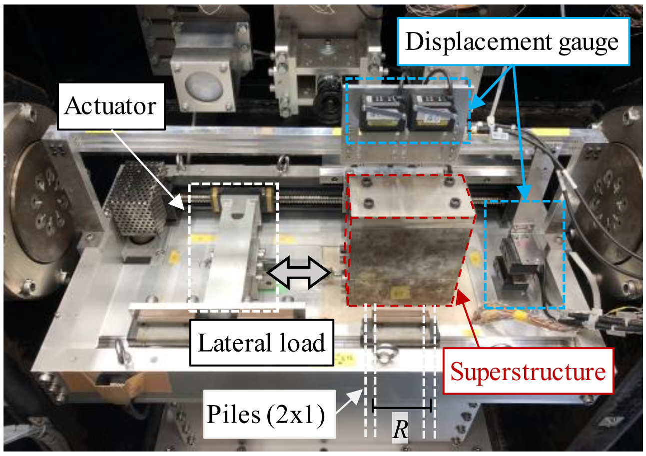

Figure 1. Set up of the test specimen

Table 1. Test specimen specifications

D **[mm]**	***t*** **[mm]**	***l*** **[m]**	***R*** **[m]**	***h*** **[m]**	***N₀*** **[kN]**
800	40	17.5	5.6	1.0	8034

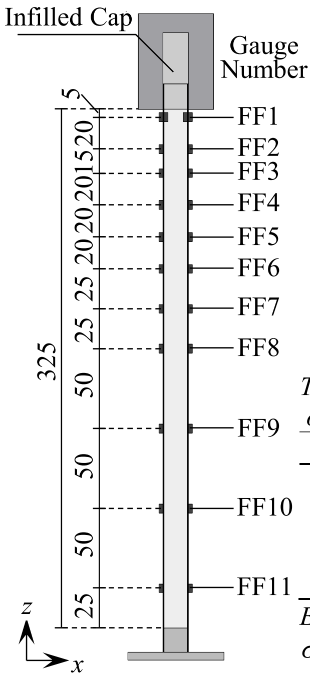

Figure 2. Strain-gauge distribution

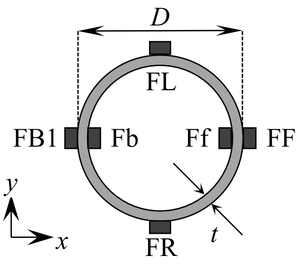

Figure 3. Cross section of pile

Table 2. Material properties of pile

Properties	
E [N/mm^2]	6.9×10^4
σ_l [N/mm^2]	205
σ_y [N/mm^2]	250
σ_u [N/mm^2]	276

E: Young's modulus
σ_l: Proportional limit stress
σ_y: Yield stress
σ_u: Tensile strength

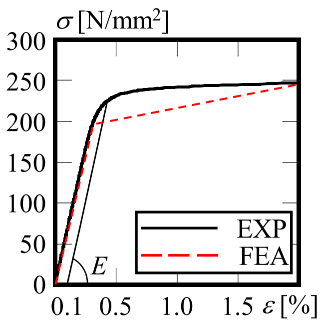

Figure 4. Stress-strain curve

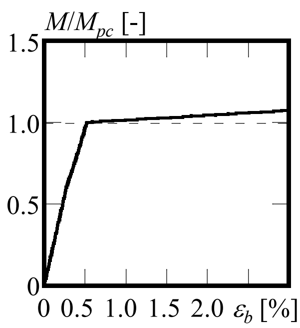

Figure 5. Skeleton curve of M/M_{pc}-ε_b

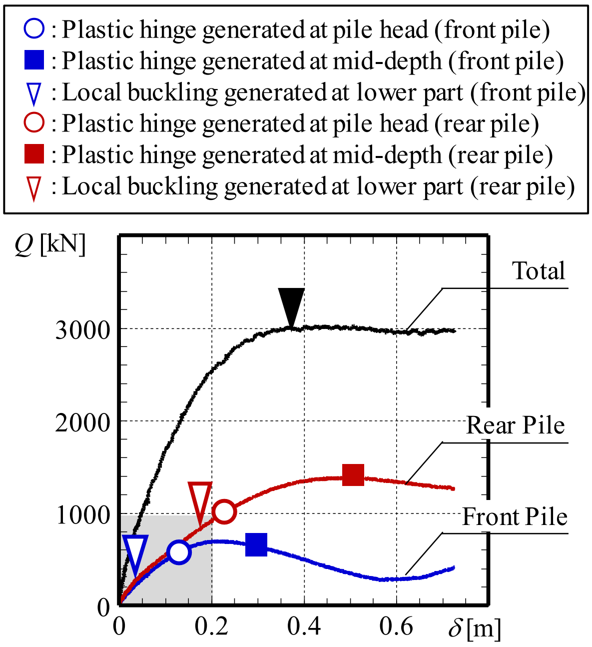

(a) Full hysteresis curve

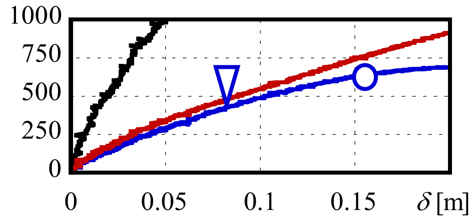

(b) Enlarged part of the initial loading stage
Figure 6. Hysteresis curve of test results

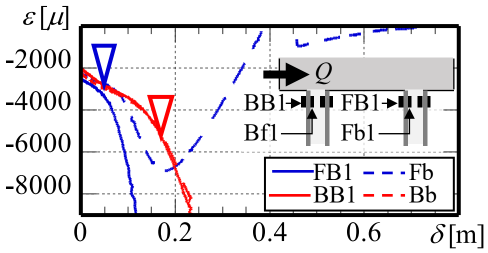

Figure 7. Progression of local buckling strain

front and rear sides of the front pile are referred to as the FF and FB series, respectively, while those on the front and rear sides of the rear pile are referred to as the BF and BB series. The gauge numbers were assigned sequentially from 1 to 11 from the pile head downward. The strain gauges were densely arranged near the pile head, where large bending moments were expected to occur. Figure 3 shows the pile cross section at the position of gauge No. 1. The dimensions are given in model scale. To detect the occurrence of local buckling, strain gauges were also attached to the inner surface of the pipe. In addition, strain gauges were placed in the direction perpendicular to the loading direction. The general

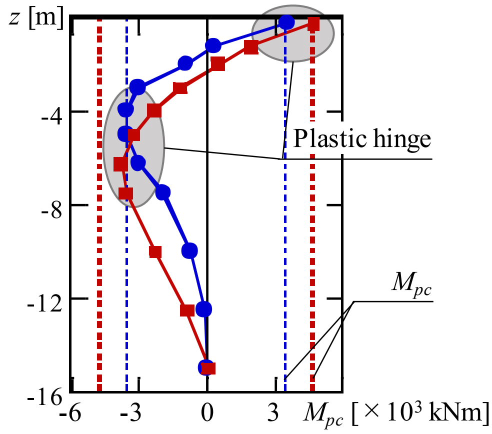

Figure 8. Bending moment distribution at ultimate lateral resistance

properties of the piles are summarized in Table 1, and all values are converted to the prototype scale. The parameters are defined as follows: D is the pile diameter; t is the pile wall thickness; l is the pile length; R is the center-to-center pile spacing; h is the loading height; and N_0 is the initial axial force per pile.

Table 2 and Figure 4 present the mechanical properties of the pile material. Here, E denotes Young's modulus, σ_l the proportional limit stress, σ_y the yield stress, and σ_u the tensile strength. σ_l was determined visually from the stress–strain curve shown in Figure 4 as the point where the hysteresis curve deviated from the elastic slope. Because the test material exhibited a round-house type stress–strain curve without a clear yield point, σ_y was defined using the 0.1% offset method. Note that the red dashed line shown in Figure 4 represents the stress-strain relationship input into the FEA model described later in Figure 11.

Figure 5 presents the normalized skeleton curve of bending moment and bending strain. The horizontal axis represents the bending strain at each position along the pile, and the vertical axis represents the bending moment normalized by the fully plastic bending moment M_{pc}, which accounts for axial force. Using this backbone curve, bending strains obtained from the strain gauges were converted into bending moments. This backbone curve was prepared with reference to the previous study (Sato et al., 2025). Unless otherwise specified, all physical quantities hereafter are expressed in prototype scale.

2.2 Loading Test Results

Figure 6 presents the relationship between applied load and lateral displacement, as well as the load carried by each pile. Here, Q denotes the shear force. "Total" represents the measured value from the load cell, while "Front Pile" and "Rear Pile" represent the shear forces at the heads of the front and rear piles, respectively. The pile head shear forces were calculated from the bending moment gradient between gauges No. 2 and No. 3. Gauge No. 1, which was located closest to the pile head, exceeded its measurement range at an early stage due to the occurrence of local buckling, and was therefore excluded from the stress calculation. Figure 6(a) shows the complete loading history, while Figure 6(b) is an enlarged view of the initial range (the shaded region in Figure 6(a)). The marks in Figure 6(a) indicate the major events that occurred during loading. The timing of local buckling and plastic hinge formation was determined from Figures 7 and 8, respectively.

From Figure 6(b), it is observed that both the front and rear piles carried nearly the same lateral load at the early stage of loading. Subsequently, after local buckling occurred in the front pile, its load-carrying capacity decreased below that of the rear pile. This behavior supports the motivation described in Chapter 1. As deformation progressed, two plastic hinges formed at approximately $\delta \approx 0.2$ m, and the lateral load carried by the piles began to decrease.
Figure 7 shows the strain histories on the front surfaces of both piles at gauge No. 1. At $\delta = 0.05$ m, a divergence between the strains measured on the outer and inner surfaces of the front pile was observed. When the Bernoulli–Navier hypothesis holds, the strains on both surfaces should coincide. However, when geometric nonlinearity such as local buckling occurs within the cross section, this assumption no longer holds, resulting in a difference between the two strains. In this study, the point at which this divergence appeared was identified as the timing of local buckling occurrence.

Figure 8 presents the bending moment distribution of the piles at the time when the ultimate lateral resistance was reached. The vertical dashed line indicates the fully plastic bending moment M_{pc}, which accounts for the axial force acting on the pile. The position where the bending moment reached M_{pc} was defined as the point of plastic hinge formation. Two plastic hinges formed in both piles, indicating that the entire system reached its ultimate state. M_{pc} was calculated using the following equation.

$$M_{pc} = \sigma_y \cdot Z_p \cdot cos\left\{\frac{\pi}{2}\left(1 - \frac{(N_F or N_R)}{N_y}\right)\right\} \quad (1)$$

Here, M_p is the full plastic bending moment, σ_y is the yield stress, Z_p is the plastic section modulus, N_y is the yield axial force, and N_F and N_R are the axial forces carried by the front and rear piles, respectively. In the calculation shown in Figure 8, these axial forces were determined from the strains measured at Gauges No. 8–10 at the ultimate lateral resistance.

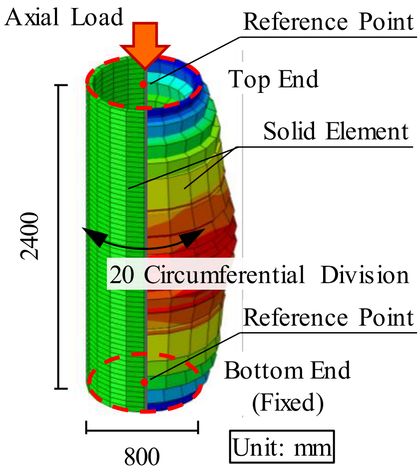

Figure 9. Overview of elastic eigenvalue analysis and elastic buckling load

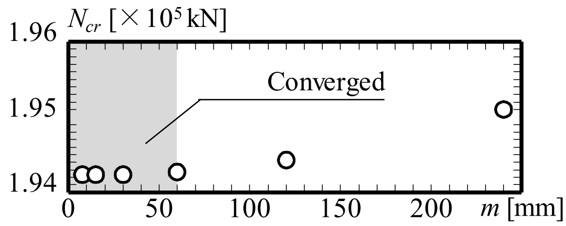

Figure 10. Relationship between mesh size and N_{cr}

3 DEVELOPMENT OF FEA MODEL

This chapter describes the development of an FEA model to reproduce the results of the loading tests presented in Chapter 2. The commercial finite element analysis software Abaqus (Dassault Systèmes, 2025) was used for the analysis.

3.1 Examination of Mesh Division

The mesh density required to reproduce local buckling behavior in the finite element analysis was examined to avoid overestimating the load due to excessive strain energy when the mesh size is too large relative to the actual buckling wavelength. An elastic buckling eigenvalue analysis was carried out to evaluate an appropriate mesh division. Figure 9 shows the analysis model and the first buckling mode. Following a previous short-column test study (Kimura et al., 2001), the specimen length was set to three times the pile diameter, and the pipe was modeled using solid elements. Reference points were placed at both ends, with all degrees of freedom of the end nodes coupled to these points. The bottom end was fully fixed, and the top end was fixed in all directions except for the loading direction. The first buckling mode was used to determine a sufficiently fine mesh size that provides a smooth mode shape representing the actual behavior.

Figure 10 presents the results of the elastic eigenvalue analysis. The vertical axis represents the elastic buckling load N_{cr}, and the horizontal axis represents the mesh size m along the pile length per element. The circumferential direction was divided into 20 segments in all models. The results show that N_{cr} asymptotically approached a constant value when m < 60 mm. In other words, using a mesh size larger than 60 mm would lead to an overestimation of the buckling load compared with the actual phenomenon.

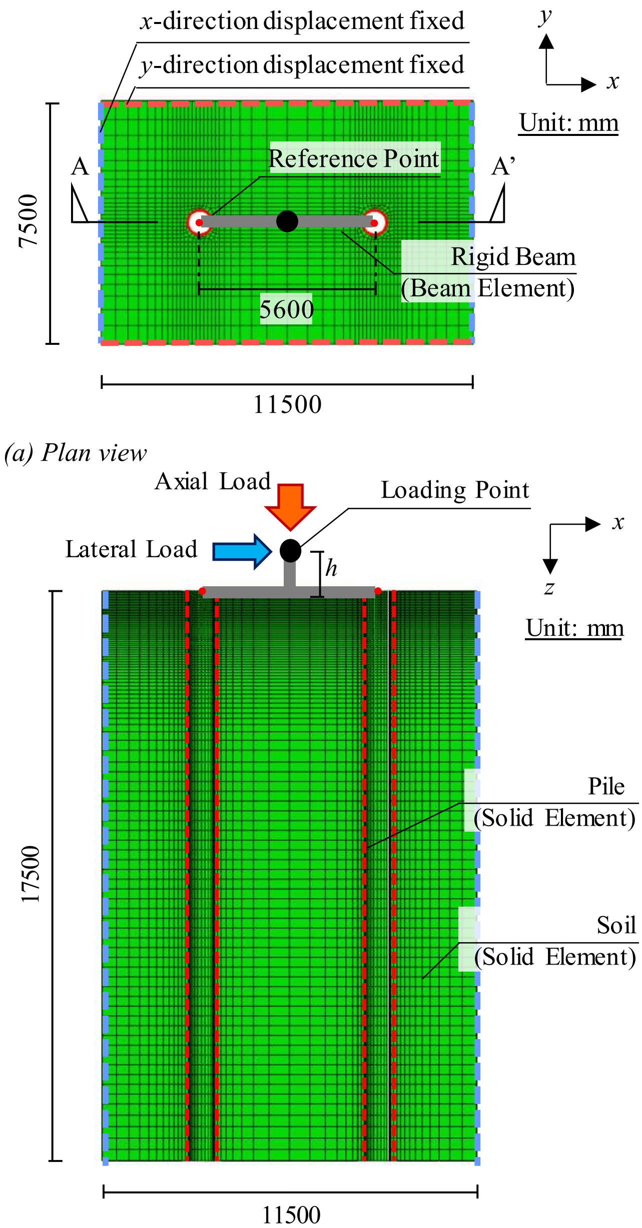

(a) Plan view

(b) Section A–A'

Figure 11. Overview of FEA model for the soil–pile–superstructure system

3.2 Overview of the FEA Model

Figure 11 illustrates the FEA model of the soil–pile–superstructure system. Figure 11(a) shows the top view, and Figure 11(b) shows the cross section along A–A'. The model consists of the soil, two piles, and the superstructure. As shown in Figure 11(a), reference points were defined at the pile heads and coupled with the corresponding pile-head nodes. Each reference point was connected by rigid beams, and a rigid column was placed at the center of the beam assembly. External lateral loads were applied at the top of the rigid column. The height of this loading point (column head height) is referred to as h. Both the rigid beams and the rigid column were modeled using beam elements. Boundary conditions were applied to the side surfaces of the soil so that no displacement occurred in the normal direction. As shown in Figure 11(b), both the soil and the piles were modeled using solid elements. The mesh division along the depth direction was kept the same for the soil and the piles. Based on the results in Figure 10, the element size was set to approximately 30 mm for a depth of about 800 mm from the ground surface to ensure sufficient resolution near the pile head. Contact was defined between the soil and the pile surfaces using the penalty method, with a friction coefficient of 0.3 assigned between the interfaces.

The soil material properties were defined using the Mohr-Coulomb model. As described in Chapter 2, although the relative density Dr was uniform, the soil was prepared in 12 layers. The FEA model was therefore divided into 12 layers as well, and layer-

Table 3 Properties of each soil layer

Layer No.	layer thickness T_l [mm]	E_0 [N/mm^2]
1	750	2.03
2	1500	2.56
3	1500	3.09
4	1500	3.62
5	1500	4.15
6	1500	4.68
7	1500	5.21
8	1500	5.74
9	1500	6.27
10	1500	6.80
11	1500	7.32
12	1500	7.94

Table 4 Common soil properties

Property	Value
Relative density Dr [%]	40
Unit weight γ [kN/m^3]	12.78
Internal friction angle ϕ [°]	35.7
Cohesion c [N/mm^2]	0.0008

specific material properties were assigned accordingly. Table 3 summarizes the physical properties of each layer. Here, E_0 represents the initial stiffness of the soil's *p*–*y* curve, which was calculated using Equation (2), where N_{SPT} is the number of blows in the standard penetration test. E_0 was assigned as the Young's modulus for each layer in the FEA model. N_{SPT} in Equation (2) was determined from Equation (3) (Gibbs and Holtz, 1957). Here, σ_v denotes the overburden pressure, which was evaluated at each depth. Table 4 lists the physical properties common to all layers. The internal friction angle ϕ was determined using Equation (4). This equation expresses the relationship between ϕ and the relative density Dr for Toyoura sand (Fujita et al., 2006), but it was also applied to the Toki silica sand No. 7 used in this study. The cohesion c was assigned a sufficiently small value, following the reference by Kashiwa et al. (Kashiwa et al., 2010), so that its effect could be neglected in the analysis.

$$E_0 = N_{SPT} \cdot 700 \tag{2}$$

$$N_{STP} = 1.7(Dr/100)^2 \cdot (0.145\sigma_v + 10) \tag{3}$$

$$\varphi = Dr \cdot 0.18 + 28.5 \tag{4}$$

3.3 FEA–Experiment Comparison

The FEA was performed under the conditions described above. The analysis steps consisted of initial → self-weight application to the soil → axial load application to the superstructure → lateral loading. Figure 12 compares the experimental and FEA results. In Figure 12(a), the solid lines represent the experimental results shown in Figure 6, while the dashed lines indicate the FEA results. The total load–displacement response showed good agreement between the experiment and the analysis. The load-sharing behavior of each pile also exhibited good correspondence. In the FEA, the pile loads were extracted at positions corresponding to the midpoint between gauges No. 2 and No. 3 to match the experimental measurement conditions.

The FEA model exhibited slightly higher stiffness than the experimental results. This difference is attributed to localized loosening of the soil near the pile surface in the experiment, where strain gauges were attached, resulting in a local reduction of Dr below 40%. Nevertheless, the overall hysteretic shape and the relative magnitudes of load sharing between the piles agreed well between the experiment and analysis.

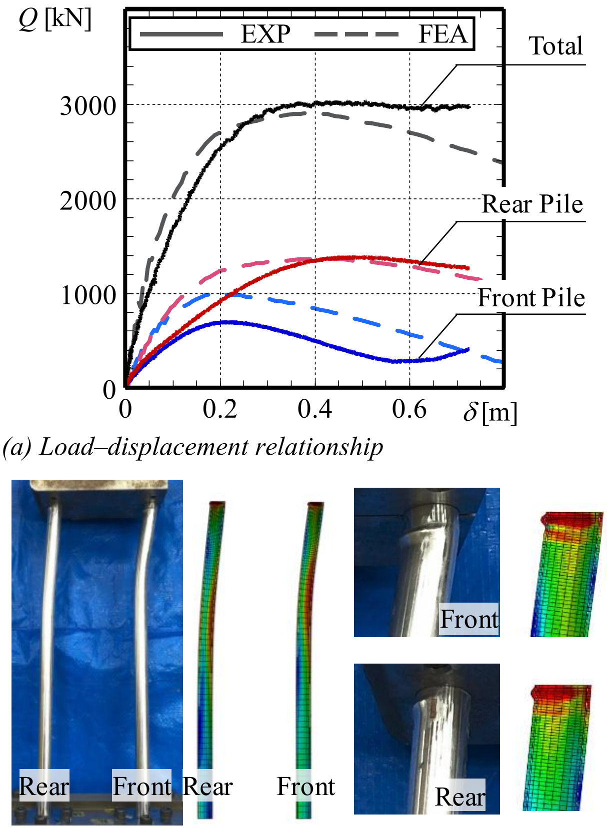

(a) Load–displacement relationship

(b) Overall deformation

(c) Local buckling at the pile head

Figure 12. Comparison between experimental and FEA results

Table 5. Parametric Study List

No.	*h* [m]	N_0/N_y [-]
3m_0.2	3	0.2
3m_0.4	3	0.4
3m_0.6	3	0.6
6m_0.2	6	0.2
6m_0.4	6	0.4
6m_0.6	6	0.6
9m_0.2	9	0.2
9m_0.4	9	0.4
9m_0.6	9	0.6

3m_0.4
Axial force ratio N_0/N_y
Loading height *h*

Figure 12(b) and (c) compares the final deformed shapes of the experimental specimen and the FEA model at the same displacement. Figure 12(b) shows the overall deformation of the piles, and Figure 12(c) provides an enlarged view near the pile heads. In the experiment, significant residual deformation was observed in the front pile subjected to larger compressive force. This behavior was also reproduced in the FEA. Moreover, residual local buckling patterns were observed in both the front and rear piles, and similar buckling deformation patterns

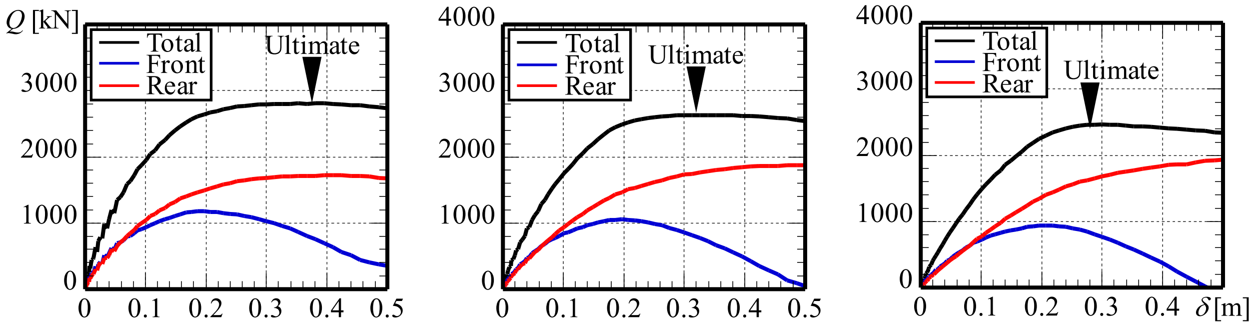

(a) 3_0.4 (b)6_0.4 (c)9_0.4

Figure 13. Comparison of load–displacement relationships at different loading heights

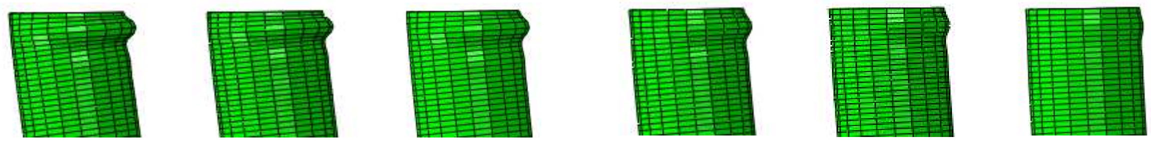

3m_0.4 6m_0.4 9m_0.4 3m_0.4 6m_0.4 9m_0.4

(a) Front Pile (b) Rear Pile

Figure 14. Comparison of pile-head local buckling at different loading heights

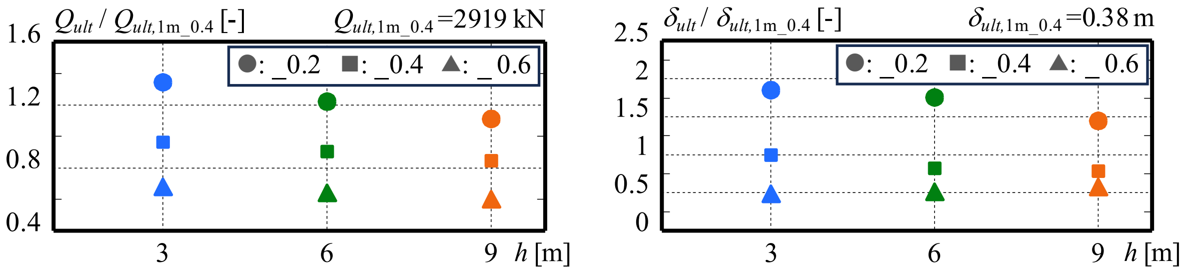

(a) Ultimate Lateral Resistance (b) Ductility

Figure 15. Trend of Structural Performance with Varying Loading Height

were reproduced in the FEA results. These comparisons demonstrate that the proposed FEA model has sufficient mesh resolution to capture the local buckling deformation observed in the experiment and can accurately reproduce the mechanical behavior of the superstructure–pile–soil system, including stress distribution and deformation characteristics.

4 PARAMETRIC STUDY

In this chapter, a parametric study was conducted using the FEA model developed in the previous chapter. The parameters were the loading height h and the axial force ratio, and their effects on the ultimate lateral resistance of the superstructure–pile–soil system and the load sharing between the piles were examined. Table 5 lists the analysis cases performed. The pile spacing and cross-sectional dimensions were kept constant in all cases.

Figure 13 presents the load–displacement relationships and the lateral loads carried by each pile for selected cases. Here, Q denotes the lateral load acting at the loading point and the load carried by each pile. In the following discussion, the lateral loads of the piles are obtained from the pile head elements without considering the strain gauge locations used in the experiment. The horizontal displacement δ represents the displacement at the loading point. The ultimate lateral resistance Q_{ult} and its corresponding displacement δ_{ult} for each case were as follows: 3m_0.4 - Q_{ult} = 2809 kN, δ_{ult} = 0.38 m; 6m_0.4 - Q_{ult} = 2633 kN, δ_{ult} = 0.31 m; 9m_0.4 - Q_{ult} = 2464 kN, δ_{ult} = 0.30 m. The maximum load carried by the front pile was defined as $_{f}Q_{ult}$, and the load carried by the rear pile at the same stage was defined as $_{r}Q_{fQult}$. The ratios $_{f}Q_{ult}$ / $_{r}Q_{fQult}$ were 0.81, 0.75, and 0.69 for 3m_0.4, 6m_0.4, and 9m_0.4, respectively. These results indicate that larger overturning moments reduce the load-carrying capacity of the front pile.

Figure 14 compares the local buckling patterns at th e pile heads at the ultimate lateral resistance for the models shown in Figure 13. Figure 14(a) shows the front pile, which experienced increased compression due to the overturning moment, while Figure 14(b) shows the rear pile, which experienced reduced compression. The front piles in all models exhibited nearly the same degree of local buckling. In contrast, the rear piles exhibited less developed buckling as the loading height h increased. This behavior suggests that the uplift force induced by the overturning moment of the superstructure acts to relieve local buckling at the pile head.

Figure 15 shows Q_{ult} and δ_{ult} for the series of parameters listed in Table 5. Each value was normalized by the results of the case with $h = 1$ m and an axial force ratio of 0.4, which corresponds to the experimental conditions. Overall, both Q_{ult} and δ_{ult} decreased monotonically as h increased. However, for the series with an axial force ratio of 0.6, δ_{ult} exhibited a slight increase with increasing h.

5 CONCLUSIONS

In this study, centrifuge loading tests were conducted on a superstructure–pile–soil system. The experiments successfully reproduced the collapse process of steel pipe piles involving local buckling. Furthermore, an FEA model capable of reproducing the experimental results was developed, and a parametric study was performed. The main findings are summarized as follows:

1. The front pile, which was subjected to higher compression due to overturning moments, exhibited a reduced load-carrying ratio compared with the rear pile because of the occurrence of local buckling, even while the material remained in the elastic range.
2. By adjusting the element size so that the lowest elastic buckling eigenvalue was obtained, the FEA model successfully reproduced a smooth local buckling pattern consistent with the experimental observations.
3. The parametric study revealed that increasing the loading height led to a decrease in both the ultimate lateral resistance of the system and the corresponding displacement.

In addition, the axial force transmitted from the superstructure to the piles through overturning moments is expected to be influenced by pile spacing. A systematic investigation considering pile spacing as a variable will be addressed in future work. The extent of local buckling is also affected by the pile cross section, particularly the diameter-to-thickness ratio. The influence of this parameter will be further examined in subsequent studies.

REFERENCES

Architectural Institute of Japan (Ed.). (2001). *Recommendations for Design of Building Foundations* (2nd ed.). [in Japanese]

Architectural Institute of Japan (Ed.). (2019). *Recommendations for Design of Building Foundations* (3rd ed.). [in Japanese]

Dassault Systèmes. (2025). *Abaqus 2025 Documentation*. Version 6.25-1. Dassault Systèmes Simulia Corp., Johnston, RI, USA.

Fujita, K., Ohno, M., Sandanbata, I., & Matsumoto, K. (2006). Relationship between relative density, internal friction angle, overburden pressure, N100-value and shearing strength. *Proceedings of the Japan National Conference on Geotechnical Engineering*, 41, 459–460. [in Japanese]

Gibbs, H. J., & Holtz, W. G. (1957). Research on determining the density of sands by spoon penetration testing. Proceedings of the 4th International Conference on Soil Mechanics and Foundation Engineering, 1, 35–39.

Kashiwa, H., Kurata, T., Hayashi, Y., Tamura, S., & Suita, K. (2007). Amplitude dependence of pile-group effect in large-amplitude lateral loading tests. *Journal of Structural and Construction Engineering* (*Transactions of AIJ*), 72(614), 53–60. https://doi.org/10.3130/aijs.72.53_1 [in Japanese]

Kashiwa, H., Shouji, M., & Hayashi, Y. (2010). Method for estimating lateral soil-spring stiffness at pile heads for pile groups, considering strong nonlinearity of pile–soil systems in sand. *Journal of Structural and Construction Engineering* (*Transactions of AIJ*), 75(651), 957–965. https://doi.org/10.3130/aijs.75.957 [in Japanese]

Kimura, Y., Ogawa, T., & Saeki, E. (2001). Local buckling behavior of cold-formed circular tubes produced by different manufacturing processes. *Steel Construction Engineering*, 8(29), 27–34. https://doi.org/10.11273/jssc1994.8.27 [in Japanese]

Kimura, Y., Yamanishi, O., & Kasai, K. (2013). Repeated axial-force behavior and residual strength of H-shaped steel beams under alternating axial loading. *Journal of Structural and Construction Engineering* (*Transactions of AIJ*), 78(689), 1307–1316. https://doi.org/10.3130/aijs.78.1307 [in Japanese]

Mukai, T., Hirada, T., Watanabe, H., et al. (2019). Study on structural performance evaluation for concrete pile sub-assemble system with post-earthquake functional use. Building Research Data No. 195. Building Research Institute, National Research and Development Agency, Japan.

National Institute for Land and Infrastructure Management (NILIM) & Building Research Institute (BRI). (2024). *Preliminary Report on Building Damage Survey for the 2024 Noto Peninsula Earthquake* (NILIM Research Report No. 1296). Ministry of Land, Infrastructure, Transport and Tourism, Tsukuba, Japan. [in Japanese]

Sato, M., & Kimura, Y. (2025). Evaluation of ultimate strength and plastic deformation capacity of steel pipe pile failed by local buckling at pile top in liquefied soil. *Soil Dynamics and Earthquake Engineering*, 198, 109544. https://doi.org/10.1016/j.soildyn.2025.109544